

AD-A060 709 NAVAL RESEARCH LAB WASHINGTON D C

THEORY AND SINGLE WAVE SIMULATION OF THE GYROTRON TRAVELING WAV--ETC(U)

AUG 78 K R CHU, A T DROBOT

UNCLASSIFIED

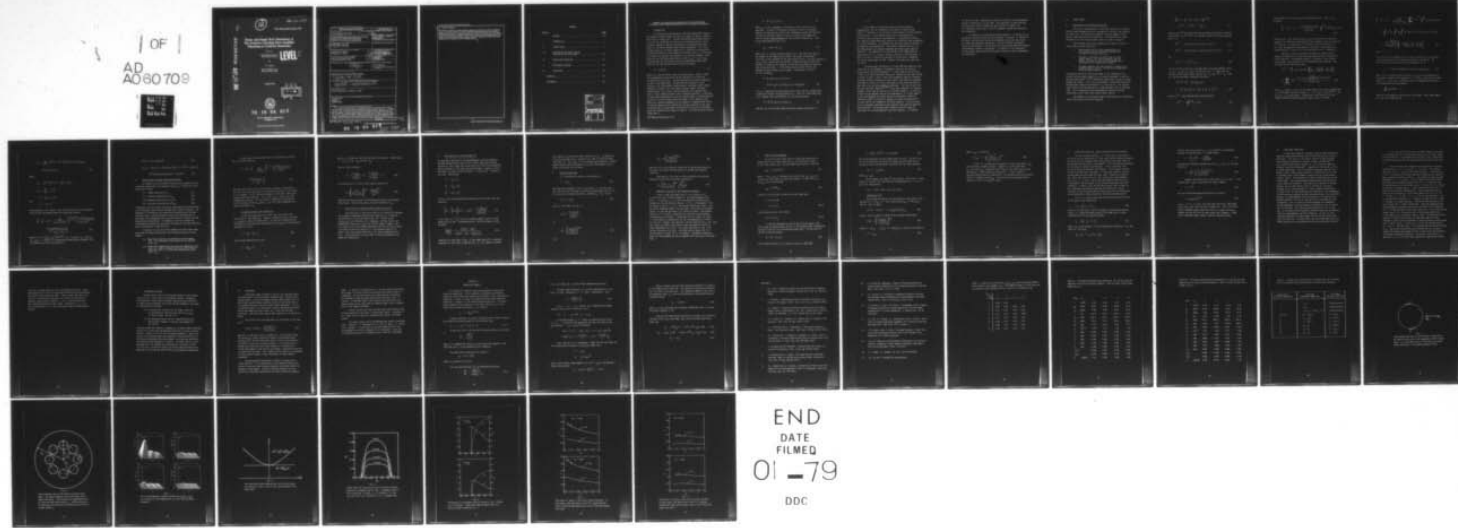
NRL-MR-3788

F/G 20/5

MIPR-FY-76-1970026

NL

SBIE-AD-E000 228



END

DATE

FILMED

01 - 79

DDC

12

Adel 000 228

NRL Memorandum Report 3788

**Theory and Single Wave Simulation of
The Gyrotron Traveling Wave Amplifier
Operating at Cyclotron Harmonics**

K. R. CHU

*Beam Applications Branch
Plasma Physics Division*

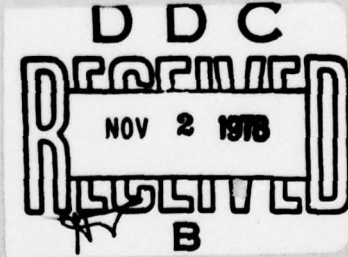
LEVEL II

AND

A. T. DROBOT

*Science Applications, Inc.
McLean, Virginia 22001*

August 1978



78 10 04 017

**NAVAL RESEARCH LABORATORY
Washington, D.C.**

SECURITY CLASSIFICATION OF THIS PAGE (When Data Entered)

REPORT DOCUMENTATION PAGE		READ INSTRUCTIONS BEFORE COMPLETING FORM
1. REPORT NUMBER NRL Memorandum Report 3788	2. GOVT ACCESSION NO.	3. RECIPIENT'S CATALOG NUMBER
4. TITLE (and Subtitle) THEORY AND SINGLE WAVE SIMULATION OF THE GYROTRON TRAVELING WAVE AMPLIFIER OPERATING AT CYCLOTRON HARMONICS,		5. TYPE OF REPORT & PERIOD COVERED Interim report on a continuing NRL problem.
6. AUTHOR(s) K.R. Chu and A.T. Drobot	7. PERFORMING ORG. REPORT NUMBER	
8. PERFORMING ORGANIZATION NAME AND ADDRESS Naval Research Laboratory Washington, D.C. 20375	9. CONTRACT OR GRANT NUMBER(s)	
10. PROGRAM ELEMENT, PROJECT, TASK AREA & WORK UNIT NUMBERS NRL Problem R18-10 Project MIPR-FY761970026	11. REPORT DATE August 1978	
12. NUMBER OF PAGES 46	13. SECURITY CLASS. (of this report) UNCLASSIFIED	
14. MONITORING AGENCY NAME & ADDRESS (if different from Controlling Office) 1247P.	15a. DECLASSIFICATION/DOWNGRADING SCHEDULE	
16. DISTRIBUTION STATEMENT (of this Report) Approved for public release; distribution unlimited. 14)NRL-MR-3788		
17. DISTRIBUTION STATEMENT (of the abstract entered in Block 20, if different from Report) 18)SBIE 19)AD-E000 228		
18. SUPPLEMENTARY NOTES *Science Applications, Inc., McLean, VA 22101		
19. KEY WORDS (Continue on reverse side if necessary and identify by block number) Cyclotron maser Harmonics Amplifier design		
20. ABSTRACT (Continue on reverse side if necessary and identify by block number) The cyclotron maser interaction in a waveguide structure at the harmonics of the cyclotron frequencies has been studied in detail both analytically and with numerical simulations. An idealized cold beam, single wave model has been assumed and investigated using the relativistic Vlasov and Maxwell equations. Analytical scaling relations for the growth rate and efficiency have been derived and extensive simulation data obtained. Emphasis has been placed on methods of parameter optimization for maximizing beam to wave energy conversion efficiency. Beam frame efficiencies in the vicinity of 20% and 10% have been found for the third and fourth cyclotron harmonics, respectively. (Continues) → next page		

DD FORM 1 JAN 73 1473 EDITION OF 1 NOV 73 IS OBSOLETE
S/N 0102-014-6601

SECURITY CLASSIFICATION OF THIS PAGE (When Data Entered)

78 10 04 017 251 950 LB

20. Abstract (Continued)

These results are capable of yielding preliminary design data for gyrotron traveling wave amplifiers. However, it should be noted that a number of important practical problems such as competition between spurious modes have not been considered in the context of the present single wave analysis. Furthermore, requirements on magnetic field uniformity and electron thermal spread become more stringent as cyclotron harmonic number increases and thus the realization of suitable experimental conditions may be expected to become increasingly difficult.

CONTENTS

<u>Section</u>		<u>Page</u>
	ABSTRACT	iii
I	INTRODUCTION	1
II	LINEAR THEORY	5
III	APPROXIMATE ANALYTICAL SCALING RELATION FOR THE EFFICIENCY	19
IV	SINGLE WAVE SIMULATION	21
V	EXPERIMENTAL DESIGNS	24
VI	DISCUSSION	25
	APPENDIX A	27
	REFERENCES	30

ACCESSION for	
NTIS	White Section <input checked="" type="checkbox"/>
DDC	Buff Section <input type="checkbox"/>
UNANNOUNCED	<input type="checkbox"/>
JUSTIFICATION _____	
BY _____	
DISTRIBUTION/AVAILABILITY CODES	
Dist. AVAIL and/or SPECIAL	
A	

THEORY AND SINGLE WAVE SIMULATION OF THE GYROTRON TRAVELING WAVE AMPLIFIER OPERATING AT CYCLOTRON HARMONICS

I. INTRODUCTION

An interesting electromagnetic radiation mechanism¹⁻³ known as the electron cyclotron maser has been the subject of intense research activities in recent years. The main motivation behind these efforts is to use this mechanism in a new class of microwave devices called gyrotrons capable of generating microwaves at unprecedented power levels at centimeter through submillimeter wavelengths. As in most microwave devices, the basic mechanism for radiation in the gyrotron is electron bunching in the presence of the wave fields. To illustrate this process we consider two electrons in an external magnetic field $B_0 \hat{e}_z$ and an oscillating wave electric field $E_x \hat{e}_x$ ($= E_0 \cos \omega t \hat{e}_x$). We assume that the two electrons have the same energy, hence they rotate on the same cyclotron orbit with the frequency

$$\Omega_c = e B_0 / \gamma m c \quad (1)$$

where γm is the relativistic mass of the electrons. Figure 1 shows the instantaneous positions of the two electrons at $t=0$ and the orientations of B_0 and E_x . The two electrons are initially separated by 180° in the phase angle. Accelerated by the electric field, electron 1 will gain energy, become heavier, and hence rotate slower. Electron 2, however, will lose energy, become lighter, and hence rotate faster. As a result, the two electrons will approach each other in their common cyclotron orbit indicating bunching. In contrast to usual bunching mechanisms, here an electron which is accelerated will actually slip back in phase angle as though it had a negative mass. Hence this bunching phenomenon can be viewed as a negative mass effect. To show how energy can be transferred from the electrons to the wave, we picture that a large number of electrons are uniformly distributed along the cyclotron orbit shown in Figure 1. The rate of total electron energy gain is

Note: Manuscript submitted June 6, 1978.

$$R = -Ne v_{cx} E_0 \cos \omega t, \quad (2)$$

where v_{cx} is the x-component of the center of mass velocity of all electrons. Initially, $R=0$ because the center of mass is stationary. However, the negative mass effect will subsequently cause the electrons to bunch so that their center of mass will shift to the right and start to rotate clockwise at the cyclotron frequency Ω_c . Thus we may approximately write v_{cx} as

$$v_{cx} = -v_0(t) \sin \Omega_c t, \quad (3)$$

where $v_0(t)$ is a slowly varying function of t . One notes that even in the absence of the negative mass effect, the center of mass would oscillate in the presence of the wave electric field. An exact expression for v_{cx} should include this oscillation as additional terms in Eq. (3). However, to simplify this example, we have only considered the negative mass contribution here. In the formal analysis which follows, the complete electron dynamics are included. Inserting Eq. (3) into Eq. (2), we obtain

$$\begin{aligned} R &= Ne v_0(t) E_0 \sin \Omega_c t \cos \omega t \\ &= \frac{1}{2} Ne v_0(t) E_0 [\sin(\Omega_c - \omega)t + \sin(\Omega_c + \omega)t]. \end{aligned} \quad (4)$$

If $\Omega_c \approx \omega$, then the first and second terms in Eq. (4) are, respectively, a slowly and rapidly varying function of t . Thus, on a slow time scale (i.e., neglect fast oscillations), Eq. (4) can be written

$$R \approx \frac{1}{2} Ne v_0(t) E_0 \sin(\Omega_c - \omega)t. \quad (5)$$

From Eq. (5), we find that negative electron energy gain occurs if

$$\omega \gtrsim \Omega_c$$

(6)

Brief summaries of gyrotron theories and experiments together with lists of references can be found in recent review papers.^{4,5} Reference 4 also contains a good summary of various gyrotron configurations. In the present study, we will concentrate on a particular type of gyrotron configurations - the gyrotron traveling wave amplifier (gyro-TWA) which consists of an electron beam propagating in a simple waveguide. As compared with the other types of gyrotrons, gyromonotron and gyrokylystron, which employ resonant cavities, the gyro-TWA generally has broader bandwidth and higher power handling capability. The operation of a gyro-TWA was first demonstrated by Granatstein,⁶ et al., using an intense relativistic electron beam. A gain of 16 dB (1.1 dB/cm) was achieved at 8.6 GHz with a bandwidth $\sim 5\%$ and an output power of 4 MW. However, efficiency was relatively low ($\lesssim 1\%$).

Cyclotron maser interactions in a gyro-TWA have generally been treated as an electromagnetic instability driven by the velocity anisotropy of the electron medium.⁷⁻¹¹ Linear theories can be found in Refs. 9-12, while nonlinear saturation mechanisms have been studied in detail in Refs. 7 and 8. While the fundamental physical processes have been carefully analyzed in these papers, the problem of parameter optimization, which is of vital importance to the actual operation of gyro-TWA's, has not been adequately addressed. This can be seen from the fact that most theories^{7,8,10,11} have been formulated in Cartesian geometry rather than the realistic cylindrical geometry. In order to bridge this gap between theories and experiments, in a recent paper¹³ we have reformulated the linear theory and developed a numerical simulation code⁸ in cylindrical geometry to study the operation of the gyro-TWA at the fundamental cyclotron harmonic. There the procedures of parameter optimization were detailed and extensive numerical data generated. The present paper contains a similar study for operations at the nonfundamental cyclotron harmonics. It presents

for the first time a comprehensive simulation study of the nonfundamental harmonic interactions in a gyro-TWA. Also analytical scaling relations for growth rate and efficiency have been derived to compare with the simulation results and to scale to parameter regimes not covered by the simulations.

In Section II, we present the linear analysis. In Section III, an analytical scaling relation for the efficiency is derived. In Section IV, we discuss the nonlinear saturation mechanisms and present the results of single wave numerical simulations. Section V applies the present theory to the design of a 94 GHz gyrotron traveling wave amplifier based on nonfundamental harmonic interactions. In Section IV, the limitations of the present theory and the difficulties involved in actual experiments are considered.

II. LINEAR THEORY

A. Derivation of the Dispersion Relation

The typical configuration of a gyro-TWA consists of an annular electron beam propagating inside a waveguide of circular cross section (of radius r_w). The electrons, guided by a uniform magnetic field ($B_0 e_z$), move along helical trajectories. The projections of these trajectories on the cross-sectional plane are shown in Figure 2.

The following simplifying assumptions are made for both the linear theory and the simulation:

1. The electrons are initially monoenergetic with their guiding centers uniformly distributed on a surface of constant radius r_0 .
2. The beam is sufficiently tenuous that its space charge electric field can be neglected and the spatial structure of the vacuum waveguide mode is unaffected by the presence of the beam.¹⁴
3. The beam interacts with the azimuthally symmetric TE waveguide mode so that all variables are independent¹⁴ of the azimuthal angle θ .

An important feature of the present model is the treatment of the electron guiding center radius r_0 as a variable parameter (in earlier parallel-plate models,^{7,8,10} the guiding centers were centrally located between the plates). This gives us the means to analytically optimize the beam-wave coupling with respect to r_0 (see item D). The electron Larmor radius has also been kept as a free parameter with no approximation. This is necessary since nonfundamental cyclotron harmonic interactions result from finite Larmor radius effects.

The dynamics of the electron beam is described by the linearized form of the relativistic Vlasov equation,

$$\left(\frac{\partial}{\partial t} + \mathbf{v} \cdot \frac{\partial}{\partial \mathbf{x}} - \frac{e}{c} \mathbf{v} \times \mathbf{B}_0 \mathbf{e}_z + \frac{\partial}{\partial p} \right) f^{(1)} = e (\mathbf{E}^{(1)} + \mathbf{v} \times \mathbf{B}^{(1)}) \cdot \frac{\partial}{\partial p} f_0 , \quad (7)$$

where f_0 and $f^{(1)}$ are the initial and perturbed distribution functions, respectively, and $\mathbf{E}^{(1)}$, $\mathbf{B}^{(1)}$ are the wave fields of the TE_{0n} waveguide mode, i.e.,

$$B_z^{(1)} = \hat{B}_z \operatorname{Re} [J_0(\alpha_n r) \exp(ik_z z - i\omega t)] , \quad (8)$$

$$B_r^{(1)} = \hat{B}_z \operatorname{Re} [-ik_z \alpha_n^{-1} J_1(\alpha_n r) \exp(ik_z z - i\omega t)] , \quad (9)$$

and

$$E_\theta^{(1)} = -\omega B_r^{(1)} / k_z c . \quad (10)$$

In Eqs. (8) thru (10), \hat{B}_z is the amplitude of the wave magnetic field, $\alpha_n \equiv x_n / r_w$, and x_n is the n -th root of $J_1(x) = 0$. Note that the validity of the linear theory requires $\hat{B}_z \ll B_0$ and $f^{(1)} \ll f_0$. From Eq. (8) and the Maxwell equations, we obtain

$$(\omega^2/c^2 - k_z^2 - \alpha_n^2) \hat{B}_z J_0(\alpha_n r) = -\frac{4\pi}{c} \exp(-ik_z z + i\omega t) \frac{1}{r} \frac{\partial}{\partial r} (r J_\theta^{(1)}) \quad (11)$$

where $J_\theta^{(1)}$ is the perturbed beam current given by

$$J_\theta^{(1)} = -e \int f^{(1)} v_\theta d^3 p . \quad (12)$$

Multiplying Eq. (11) by $rJ_0(\alpha_n r)$ and integrating over r from 0 to r_w , we obtain

$$\frac{\omega^2}{c^2} - k_z^2 - \alpha_n^2 = \frac{-8\pi\alpha_n \exp(-ik_z z + i\omega t)}{cr_w^2 J_0^2(\chi_n)} \int_0^{r_w} r J_0(1) J_1(\alpha_n r) dr , \quad (13)$$

Equations (7), (12), and (13) form a set of self consistent equations. To derive the dispersion relation from these equations, we first solve for $f^{(1)}$ from Eq. (7), then insert $f^{(1)}$ into Eq. (12) to calculate $J_\theta^{(1)}$. The final expression for the dispersion relation is then obtained by substituting $J_\theta^{(1)}$ into Eq. (13) and carrying out the r - integration.

Equation (7) can be solved by the method of characteristics, namely, by integrating it along the unperturbed (helical) trajectories of the electrons. Considerable algebra is involved in this integration; however, the procedures are straightforward and standard. Here we simply present the final result,

$$f^{(1)} = \frac{ek_z}{\alpha_n} \exp(ik_z z - i\omega t) \left[\left(\frac{\omega}{k_z c} - \frac{p_z}{\gamma mc} \right) \frac{\partial f_0}{\partial p_\perp} + \frac{p_\perp}{\gamma mc} \frac{\partial f_0}{\partial p_z} \right] \\ \cdot \sum_{s,s'=-\infty}^{\infty} (i)^{s'} \frac{J_{s'}(\alpha_n r) G_{ss'} \left(\frac{\alpha_n p_\perp}{m\Omega_e} \right) \exp[-is'(\psi - \theta)]}{\omega - k_z v_z - s\Omega_e} \quad (14)$$

where $\Omega_e \equiv eB_0/mc$, ψ and θ are the polar angles of p_\perp and r , respectively, J_s is the Bessel function of order s , $\gamma = [1 + (p_\perp^2 + p_z^2)/m^2 c^2]^{1/2}$, and $G_{ss'}(x) = J_{s+s'}(x) dJ_s(x)/dx$. Inserting Eq. (14) into Eq. (12) and substituting the resulting equation into Eq. (13), we obtain

$$\frac{\omega^2}{c^2} - k_z^2 - \alpha_n^2 = \frac{4\pi e^2}{mc^2 r_w^2 J_0^2(\alpha_n r_w)} \sum_{s,s'=-\infty}^{\infty} (i) \int_0^{r_w} r J_1(\alpha_n r) J_{s'}(\alpha_n r) dr$$

$$\cdot \int_0^{\infty} p_{\perp}^3 dp_{\perp} \int_{-\infty}^{\infty} dp_z \int_0^{2\pi} d\hat{\psi} \left\{ \exp[-i(s'-1)\hat{\psi}] - \exp[-i(s'+1)\hat{\psi}] \right\}$$

$$\cdot \frac{G_{ss'} \left(\frac{\alpha_n p_{\perp}}{m\omega_e} \right)}{\gamma\omega - k_z p_z / m - s\omega_e} \left[\left(\omega - \frac{k_z p_z}{\gamma m} \right) \frac{1}{p_{\perp}} \frac{\partial f_0}{\partial p_{\perp}} + \frac{k_z}{\gamma m} \frac{\partial f_0}{\partial p_z} \right] , \quad (15)$$

where $\hat{\psi} \equiv \psi - \theta$.

To carry out the r -integration in Eq. (15), we need to first construct a distribution function f_0 from the constants of the motion. The distribution function consistent with assumption (i) is

$$f_0 = K \delta(r_L^2 - 2c p_{\theta}/eB_0 - r_0^2) \delta(p_{\perp} - p_{\perp 0}) \delta(p_z - p_{z0})/p_{\perp} , \quad (16)$$

where $\delta(x)$ is the Dirac delta function, $p_{\perp 0}$, p_{z0} are the perpendicular and parallel momenta of the electrons, $r_L \equiv p_{\perp}/m\omega_e$ is the electron Larmor radius, $p_{\theta} = \gamma m r p_{\perp} \cos \hat{\psi} - eB_0 r^2/2c$, and K is a normalization constant to be determined from the equation

$$\int f_0 2\pi r dr d^3p = N$$

where N is the number of electrons per unit length. After some algebra, Eq. (16) can be rewritten as

$$f_0 = \frac{N}{2\pi^2 p_\perp} [\delta(\hat{\psi} - \hat{\psi}_0) + \delta(\hat{\psi} - \pi + \hat{\psi}_0)] \delta(p_\perp - p_{\perp 0}) \delta(p_z - p_{z 0}) \\ \bullet S(r - r_1) S(r_2 - r) , \quad (17)$$

where

$$\hat{\psi}_0 = \sin^{-1} [(r^2 + r_L^2 - r_0^2) / 2rr_L] ,$$

$$S(x) = \begin{cases} 1, & x \geq 0 \\ 0, & x < 0 \end{cases}$$

$$r_1 = |r_0 - r_L| ,$$

and

$$r_2 = r_0 + r_L .$$

Substituting Eq. (17) into Eq. (15), we can carry out all the integrations exactly and thereby obtain the dispersion relation

$$\frac{\omega^2}{c^2} - k_z^2 - \alpha_n^2 = \frac{-4v}{\gamma_0 r_w^2 J_0^2(\alpha_n r_w)} \left[\frac{(\omega^2 - k_z^2 c^2) \beta_{\perp 0}^2 H_s(\alpha_n r_0, \alpha_n r_L)}{(\omega - k_z v_{z 0} - s\Omega_c)^2} \right. \\ \left. - \frac{(\omega - k_z v_{z 0}) Q_s(\alpha_n r_0, \alpha_n r_L)}{(\omega - k_z v_{z 0} - s\Omega_c)} \right] , \quad (18)$$

where $\gamma_0 = [1 + (p_{\perp 0}^2 + p_{z 0}^2)/m^2 c^2]^{1/2}$, $\beta_{\perp 0} = p_{\perp 0}/\gamma_0 m c$, $v_{z 0} = p_{z 0}/\gamma_0 m$, $\Omega_c = \Omega_e/\gamma_0$, $v = Ne^2/mc^2$ is a dimensionless beam density parameter, and the functions H_s and Q_s are defined as

$$H_s(x, y) \equiv [J_s(x)J_s'(y)]^2 \quad (19)$$

$$Q_s(x, y) \equiv 2H_s(x, y) + yJ_s'(y)J_s''(y) \{ J_s^2(x)(1 + s^2/x^2) + [J_s'(x)]^2 \} \\ + 2s^2 J_s(x)J_s'(x)J_s'(y)[yJ_s'(y) - J_s(y)]/xy \quad (20)$$

B. Normalization and Beam Frame Representation

For generality, the following normalization procedures will be introduced through which the waveguide radius r_w is scaled out of the dispersion relation:

(i) Length normalized to r_w , (21)

(ii) Frequency normalized to c/r_w , (22)

(iii) Momentum normalized to mc , and (23)

(iv) EM fields normalized to $mc^2/\epsilon r_w$. (24)

Furthermore, we will present the results, both analytical and numerical, in the reference frame in which the beam axial velocity vanishes. The advantage for introducing the normalization procedures and the beam reference frame is that the numerical data to be presented will be applicable to any waveguide radius and any beam axial velocity through appropriate transformations. In Appendix A, we have included the transformation formulae for conversion from beam to lab frame quantities and from normalized to physical units.

To maintain a clear distinction between lab frame, beam frame, normalized and physical quantities, the following notation has been adopted:

(i) Beam frame quantities are denoted by primed symbols (e.g., γ'), laboratory frame quantities are unprimed (e.g., γ_0).

(ii) Normalized dimensionless quantities are denoted by a bar (e.g., $\bar{\omega}$). Unbarred symbols represent either physical quantities (e.g., ω) or naturally dimensionless ones (e.g., γ_0).

In beam frame, the normalized form of the dispersion relation [Eq. (18)] can be written

$$\bar{\omega}'^2 - \bar{k}_z'^2 - x_n^2 = \frac{-4\gamma'_0}{\gamma'_0 J_0^2(x_n)} \left[\frac{(\bar{\omega}'^2 - \bar{k}_z'^2) \beta_{10}'^2 H_s(x_n \bar{r}_0, x_n \bar{r}_L)}{(\bar{\omega}' - s\bar{\Omega}'_c)^2} \right. \\ \left. - \frac{\bar{\omega}' Q_s(x_n \bar{r}_0, x_n \bar{r}_L)}{\bar{\omega}' - s\bar{\Omega}'_c} \right], \quad (25)$$

Note that the primes in Eqs. (19) and (20) represent, respectively, the first and second derivatives of the Bessel function J_s with respect to its argument. In Eq. (25) and elsewhere in this paper, the primes indicate beam frame quantity. In Eq. (25), \bar{r}_0, \bar{r}_L , and x_n are frame independent quantities. It can be easily shown that the normalized cutoff frequency of the TE_{on} mode, $\bar{\omega}_c$, is also frame independent and numerically equal to x_n .

C. Threshold Condition for Instability

On the right hand side of Eq. (25), the first term is the source term of the instability. However, instability occurs only when β_{10}' exceeds a certain threshold value. To find this threshold value, we expand Eq. (25) about the intersecting point $(\bar{\omega}_0', \bar{k}_{z0}')$ of the waveguide characteristic curve

$$\bar{\omega}'^2 - \bar{k}_z'^2 - x_n^2 = 0, \quad (26)$$

and the beam characteristic curve

$$\bar{\omega}' - s\bar{\Omega}'_{co} = 0, \quad (27)$$

where Ω_{co} is chosen so that the two curves do intersect. Substituting $\bar{\omega}' = \bar{\omega}_0 + \Delta\bar{\omega}'$, $\bar{k}'_z = \bar{k}'_{z0}$, and $\bar{\Omega}'_c = \bar{\Omega}'_{co}$

into Eq. (25), we obtain

$$\Delta\bar{\omega}'^3 - \frac{2v's\bar{\Omega}'_{co}Q_s}{\gamma_0\bar{\omega}'_0J_0^2(x_n)} \Delta\bar{\omega}' + \frac{2v'x_n^2H_s\beta'_{10}^2}{\gamma_0\bar{\omega}'_0J_0^2(x_n)} = 0. \quad (28)$$

The condition for Eq. (28) to have complex solutions is

$$\beta'_{10} > \left[\frac{8v'}{27\gamma_0\bar{\omega}'_0J_0^2(x_n)} \right]^{1/4} \frac{(s\bar{\Omega}'_{co}Q_s)^{3/4}}{x_nH_s^{1/2}}. \quad (29)$$

Equation (29) can be solved for the threshold velocity for unstable interactions. Note that Q_s and H_s are both functions of β'_{10} .

D. Optimization of the Beam Guiding Center Position \bar{r}_0

The function H_s in the source term of the instability indicates the strength of beam-wave coupling with respect to \bar{r}_0 . A physical interpretation of H_s can be found in Ref. 15. Figure 3 plots $H_s(x_n\bar{r}_0, x_n\bar{r}_L)$ as a function of its arguments. We note that H_s is a nonmonotonic function of \bar{r}_0 with an infinite number of peaks. The first peak of H_s has the highest amplitude, thus the value of \bar{r}_0 which corresponds to the first peak of H_s is the optimum choice for \bar{r}_0 . Table I lists the optimum values of \bar{r}_0 for various combinations of s and n . These values will be used later in selecting parameters for numerical computations.

E. Optimization of the Wave Number \bar{k}'_z

For gyro-TWA's operating at the nonfundamental cyclotron harmonics the beam energy (usually tens of keV) is well above the threshold given by Eq. (23), hence the second term of Eq. (25) can be neglected. Again we expand Eq. (25) about the point $(\bar{\omega}'_0, \bar{k}'_{z0})$. However, we will now expand in terms of three variables - $\bar{\omega}'$, \bar{k}'_z and $\bar{\Omega}'_c$ - instead of just one. Substituting

$$\bar{\omega}' = \bar{\omega}'_0 + \Delta\bar{\omega}'$$

$$\bar{k}'_z = \bar{k}'_{z0} + \Delta\bar{k}'_z$$

$$\bar{\Omega}'_c = \bar{\Omega}'_{co} + \Delta\bar{\Omega}'_c$$

into Eq. (25) and neglecting the second term on the right hand side, we obtain

$$\left[\frac{\bar{k}'_{z0}}{\bar{\omega}'} \frac{\Delta\bar{k}'_z}{\Delta\bar{\omega}'} \right] (\Delta\bar{\omega}' - s\Delta\bar{\Omega}'_c)^2 = \frac{-2v' x_n^2 H_s \beta_{z0}^2}{\gamma_0 J_0^2 (x_n) \bar{\omega}'_0} , \quad (30)$$

In Eq. (30), $\Delta\bar{\omega}' = \Delta\bar{\omega}'_r + i\Delta\bar{\omega}'_i$ is a complex number, while all other quantities are real. Differentiating Eq. (30) with respect to $\Delta\bar{k}'_z$, we obtain

$$\frac{d(\Delta\bar{\omega}')}{d(\Delta\bar{k}'_z)} = \frac{\bar{k}'_{z0}(\Delta\bar{\omega}' - s\Delta\bar{\Omega}'_c)}{\bar{\omega}'_0(3\Delta\bar{\omega}' - s\Delta\bar{\Omega}'_c - 2\bar{k}'_{z0}\Delta\bar{k}'_z/\bar{\omega}'_0)} \quad (31)$$

Equation (31) shows that if $\bar{k}'_{z0} = 0$, the growth rate $\Delta\bar{\omega}'_i$ is a maximum regardless of the values of $\Delta\bar{k}'_z$ and $\Delta\bar{\Omega}'_c$, i.e., $\Delta\bar{\omega}'_i$ remains a maximum

with respect to \bar{k}'_z even with small variations in $\bar{\Omega}'_c$. In comparison, if $\bar{k}'_{z0} \neq 0, \bar{\omega}'_1$ peaks [i.e., the RHS of Eq. (30) is real] only when $\Delta\bar{k}'_z = \Delta\bar{\Omega}'_c = 0$. Thus, $\bar{k}'_{z0} = 0$ is an optimum choice because it insures maximum growth rate (with respect to \bar{k}'_z) when the magnetic field is varied to optimize the efficiency.

F. Maximum Growth Rate

It is convenient to define a new parameter X' :

$$X' \equiv s\bar{\Omega}'_c/X_n. \quad (32)$$

When the applied magnetic field is such that $X' = 1$ the two curves [Eq. (26) and (27)] intersect at an exact grazing angle (see Fig. 4). At the point of grazing intersection, we have $\bar{k}'_{z0} = \Delta\bar{\Omega}'_c = 0$ and

$$\bar{\omega}'_0 = x_n = s\bar{\Omega}'_{co}, \quad (33)$$

thus Eq. (30) gives, for $\Delta\bar{k}'_z = 0$,

$$(\Delta\bar{\omega}')^3 = \frac{-2v'x_n H_s \beta_{10}^{'2}}{\gamma'_0 J_0^2(x_n)},$$

or

$$\Delta\bar{\omega}'_r = \left[\frac{v'x_n H_s \beta_{10}^{'2}}{4\gamma'_0 J_0^2(x_n)} \right]^{1/3}, \quad (34)$$

and

$$\Delta\bar{\omega}_i' = \sqrt{3} \left[\frac{v' x_n H_s \beta_{10}^2}{4 \gamma_0' J_0^2(x_n)} \right]^{1/3} \quad (35)$$

Equation (35) is an analytical expression of the maximum growth for the usual case, where the beam energy far exceeds the threshold condition.

Inserting Eq. (23) into Eq. (29), we obtain the threshold condition for the case of grazing intersection

$$\beta_{10} > \left[\frac{8v'}{27 \gamma_0' J_0^2(x_n)} \right]^{1/4} \frac{Q_s^{3/4}}{x_n^{1/2} H_s^{1/2}} \quad (36)$$

G. Numerical Solutions of the Dispersion Relation

Figure 5 shows the growth rate $\bar{\omega}_i'$ as a function of \bar{k}_z' for the first four cyclotron harmonics. The beam parameters used were $v' = 0.002$ and $\gamma_0' = 1.1$, which characterize the electron gun designed for the NRL gyrotron program. In Fig. 4, the magnetic field was chosen so that $x' = 1$ (i.e., the grazing intersection case). Also the radial eigenmode number n was set equal to the cyclotron harmonic number s so that the optimized \bar{r}_0 as found from Table I (the numbers marked by "*") indicates a beam position centrally located between the waveguide axis and wall. Henceforth, we will always let n equal s in the numerical computations and the corresponding \bar{r}_0 in Table I will be used. However, the analytical scaling relations [e.g., Eqs. (34), (35), (45), and (50)] can be used to scale the numerical results to other combinations of n and s . The growth rate plots in Fig. 4 are typical solutions of Eq. (25). One notes that $\bar{\omega}_i'$ peaks at $\bar{k}_z' = 0$ and decreases as either $|\bar{k}_z'|$ or s increases. Information concerning power gain and bandwidth can also be deduced from these plots (discussed next).

H. Power Gain and Bandwidth

Let G be the total power gain of a gyro-TWA system which is characterized by a linear growth rate ω_i and interaction length L . At the linear growth rate, the wave power amplification is given by

$$P_{\text{out}} = P_{\text{in}} \exp (2\omega_i \tau) \quad (37)$$

where $\tau \equiv L/v_{z0}$, v_{z0} is the beam axial velocity and P_{in} , P_{out} are, respectively, the input and output wave powers. In terms of G , P_{in} and P_{out} are related through

$$P_{\text{out}} = 10^{G/10} P_{\text{in}}. \quad (38)$$

From Eqs. (37) and (38), we obtain the total power gain

$$\begin{aligned} G &= 20 \omega_i \tau / \ln 10 \\ &\approx 8.7 \omega_i \tau \text{ dB} \end{aligned} \quad (39.1)$$

and the power gain per unit length

$$g \approx 8.7 \omega_i / v_{z0} \quad (39.2)$$

To find the bandwidth, we let ω_i^m and ω_i^h be the growth rates which yield the maximum power and half of the maximum power, respectively, and let G^m and G^h be the corresponding power gains. By definition G^m and G^h are related through

$$G^h = G^m - 10 \log 2. \quad (40)$$

This together with Eq. (39.1) gives the ratio of ω_i^h to ω_i^m ,

$$R = \omega_i^h / \omega_i^m = G^h / G^m = 1 - 10 \log 2/G^m. \quad (40)$$

This ratio determines the half power points in the $\bar{\omega}'_i - \bar{k}'_z$ plot (see Fig. 4) and therefore the width $\Delta \bar{k}'_z$ between the half power points. Through a Lorentz transformation, we obtain the lab frame bandwidth

$$\Delta \omega / \omega \approx \beta_{z0} \Delta \bar{k}'_z / x_n, \quad (41)$$

where $\beta_{z0} = v_{z0} / c$.

As an example, we assume $G^m = 20$, hence Eq. (40) gives $R = 0.85$. From Fig. 4 and Eq. (41), we find that the bandwidth for $s = 1, 2, 3$, and 4 are, respectively

$$\Delta \omega / \omega = 11.19\%, 7.44\%, 5.11\%, \text{ and } 3.91\%.$$

I. Sensitivity to \bar{X}'

We consider the special case of grazing or near grazing interactions ($X' \lesssim 1$, $\bar{k}'_{z0} = 0$). Thus, substituting $\bar{k}'_{z0} = 0$ and $\bar{\omega}'_0 \approx x_n$ into Eq. (30), we obtain

$$\Delta \bar{\omega}' (\Delta \bar{\omega}' - s \Delta \bar{\omega}'_c)^2 = - 2v' x_n H_s \beta_{z0}^2 / \gamma_0 J_0^2 (x_n). \quad (42)$$

From Eq. (42), we obtain a condition for unstable interactions,

$$s \Delta \bar{\omega}'_c > -3 \left[\frac{v' x_n H_s \beta_{z0}^2}{2 \gamma_0 J_0^2 (x_n)} \right]^{1/3} \quad (43)$$

Since $X' = s(\bar{\omega}'_{co} + \Delta \bar{\omega}'_c) / x_n = 1 + s \Delta \bar{\omega}'_c / x_n$, Eq. (43) can be written as

$$X' > X'_{\min} \quad (44)$$

where X'_{\min} is defined as

$$X'_{\min} = 1 - 3 \left[\frac{v' H_s \beta'_{10}^2}{\gamma_0' x_n^2 J_0^2(x_n)} \right]^{1/3}. \quad (45)$$

In Sec. IV, we show that by lowering X' from unity toward X'_{\min} , the efficiency increases sharply. However, it can be shown from Eq. (39) that X_{\min} is generally very close to unit, which implies that efficiency is a very sensitive function of X' . Thus in order to optimize the efficiency by adjusting X' , one should be able to accurately control X' between 1 and X'_{\min} . This point will be discussed quantitatively in Sec. V for specific cases.

III. APPROXIMATE ANALYTICAL SCALING RELATION FOR THE EFFICIENCY

From the foregoing analysis, it is clear that a gyro-TWA can operate on various combination of s and n and involve numerous parameters. By scaling out the waveguide radius and working in the beam frame, we have generalized the results considerably. Still the remaining parameters are too many for numerical optimization. This is especially true for cases involving nonlinear calculations. In this regard, general scaling relations prove invaluable. In the linear analysis, we have already shown how the growth rate [Eq. (35)], instability threshold [Eq. (36)], and sensitivity to X' [Eq. (45)] scale with parameters such as v' , γ'_0 , n , and s . Thus, from the numerical data on one set of parameters, one can deduce fairly accurate information for other parameters. Similarly, for the nonlinear analysis that follows, we will complement the numerical approach with analytical scaling relations so that discrete numerical data points can be interpolated and extrapolated to cover essentially the entire parameter space.

In Sec. II, we have shown that the following condition holds at the onset of the instability,

$$\bar{\omega}'_r - s\bar{\omega}'_e/\gamma'_0 = \Delta\bar{\omega}'_r, \quad (46)$$

where $\Delta\bar{\omega}'_r$ is given by Eq. (28) for the case of grazing intersection and $\bar{k}'_z = 0$. Recent nonlinear analysis⁸ has shown that a similar condition holds at the saturation state,

$$\bar{\omega}'_r - s\bar{\omega}'_e/\langle \gamma'_s \rangle \approx -\Delta\bar{\omega}'_r, \quad (47)$$

where $\langle \gamma'_s \rangle$ is the average γ' of all electrons at saturation. Eq. (46) minus Eq. (47) gives

$$s\bar{\omega}'_e (\langle \gamma'_s \rangle^{-1} - \gamma'_0^{-1}) \approx 2\Delta\bar{\omega}'_r. \quad (48)$$

From Eq. (48) and assuming $\Delta\bar{\omega}_r \ll x_n$, we obtain an approximate estimate of the efficiency η' (in beam frame),

$$\eta' = \frac{\gamma'_0 - \langle \gamma'_s \rangle}{\gamma'_0 - 1} = \frac{2\gamma'_0 \Delta\bar{\omega}_r}{(\gamma'_0 - 1) s \Omega_c}. \quad (49)$$

For the case of grazing intersection ($\chi' = 1$, $x_n = s \Omega_c$), Eq. (34) and (49) give

$$\eta' = \frac{\gamma'_0}{\gamma'_0 - 1} \left[\frac{2v' H_s \beta'_{10}^2}{\gamma'_0 x_n^2 J_0^2(x_n)} \right]^{1/3}. \quad (50)$$

Equation (50) shows how η' scales with γ'_0 , s , n , and v' . The scaling with v' and n is particularly simple, namely,

$$\eta' \propto v^{1/3} \quad (51)$$

and, for the optimum beam positions given in Table I,

$$\eta' \propto [x_n J_0(x_n)]^{-2/3} \quad (52)$$

For $n = 1, 2, 3, 4$, and 5 , the right hand side of Eq. (52) equals $0.75, 0.61, 0.54, 0.49$, and 0.45 , respectively. Thus, using lower radial eigenmode numbers generally results in higher efficiency. However, we note that for the same output wave frequency, a lower radial eigenmode number implies a smaller waveguide radius.

IV. SINGLE WAVE SIMULATION

A single wave numerical simulation code has been developed to study the saturation mechanisms and calculate the energy conversion efficiency. This code is a cylindrical version of the Cartesian code originally developed by Sprangle, Drobot, and Manheimer^{7,8}. For a detailed description, see Ref. 8. The simulation shows two different saturation mechanisms⁹: depletion of free energy and loss of phase synchronism. The first mechanism dominates when the beam energy is only slightly above threshold. Saturation occurs as soon as the beam loses a small amount of energy and the system becomes linearly stable. This mechanism can lead to saturation even in the linear stage. The second mechanism dominates when the beam energy is well above the threshold. Saturation occurs because an average electron loses so much energy that its relativistic cyclotron frequency $\bar{\omega}_c$ no longer matches $\bar{\omega}_r$ to favor unstable interactions. As found in Ref. 8, both mechanisms are important for the fundamental cyclotron harmonic because the beam threshold energy is not negligible. However, for nonfundamental cyclotron harmonics, we found that the threshold energy is usually so low that the first mechanism can be disregarded. This is a basic difference between the fundamental and nonfundamental cyclotron harmonic interactions as far as saturation is concerned. The scaling relations derived in Sec. II and Sec. III by neglecting the threshold condition would thus be generally valid for nonfundamental cyclotron harmonics. In fact, all the simulation data which follows agrees with the scaling relation [Eq. (50)] to within 10%. In other words, from one single data point, all other data points can be predicted with an accuracy better than 90%.

As a cross check of the code the linear frequency and growth rate obtained from Eq. (25) have been compared to the linear stages of the simulation. The agreement was very good. Also, conservation of energy was monitored in the code and never deviated by more than 0.1%.

There are seven free parameters to be specified in making a simulation run, i.e., s , n , \bar{r}_0 , \bar{k}_z' , v' , γ_0' , and X' . For reasons described in Sec. II, we will let s and n be equal. Linear analysis of Sec. I has shown that maximum beam-wave coupling occurs when $\bar{k}_z' = 0$ and \bar{r}_0 assumes the values in Table I. Thus there are four remaining parameters: s , v' , γ_0' , and X' . We will restrict our study to the third and fourth cyclotron harmonics and let $v' = 0.002$ and 0.005 . The beam energy γ_0' will be varied from $\gamma_0' = 1.04$ to 1.5 (i.e., 20 keV to 250 keV in the beam frame). Finally, the specification of X' is based on the following consideration. Figure 6 shows two typical plots of the efficiency (η') and linear growth rate ($\bar{\omega}_i'$) vs X' for $v' = 0.005$, $\gamma_0' = 1.1$, and $s = 3, 4$. It can be seen that both η' and $\bar{\omega}_i'$ are sensitive functions of X' . However, as shown in Fig. 6, when η' increases, $\bar{\omega}_i'$ always decreases. High efficiency achieved at too low a growth rate is clearly undesirable. Thus some compromise must be made between the growth rate and the efficiency in our selection of X' . We have decided to select two values of X' : one at the maximum growth rate ($X' = 1$), the other at half of the maximum growth rate [$X' = X_h'$, where X_h' is to be found from Eq. (25)]. The efficiency calculated at $X' = X_h'$ will be referred to as the optimized efficiency, although it could still be increased if one can tolerate a lower growth rate. Figure 7 plots η' versus γ_0' for $s = 3$ and the selected values of v' and X' . One notes that η' is a monotonically decreasing function of γ_0' . We did not continue the curves through the low γ_0' region, because the growth rates become too low in that region and simulation runs become exceedingly expensive. The points at $\gamma_0' = 1.06$ and 1.1 marked by 1, 2, 3, and 4 have been selected for experimental designs

(see Sec. V) because they are close to the peak efficiency. Lower beam energies will result in even higher efficiencies, but beam power and growth rate will both be lower. Figure 8 plots the same curves for $s=4$. In contrast to the case of $s=3$, here the efficiency is generally lower and has a peak at $\gamma = 1.14$. Such differences are also predicted analytically [Eq. (50)]. The points at $\gamma_0 = 1.10$ and 1.14 marked by 5, 6, 7, and 8 have been chosen for experimental designs.

V. EXPERIMENTAL DESIGNS

We now convert each of the selected optimum or near optimum points in Figs. 7 and 8 into an experimental design. Parameters corresponding to these points are beam frame normalized quantities. To convert these parameters into actual design parameters, two pieces of information are required.

- (i) the beam axial velocity (in lab frame), which can be calculated by specifying the ratio $\alpha [\equiv v_{10} / v_{z0}]$ in the lab frame. We let $\alpha=1.5$.
- (ii) the waveguide radius, which is determined from the desired wave frequency, $f=94$ GHz, [see Appendix A, Eq. (A-4)].

Using the conversion formulae in Appendix A, we obtain eight preliminary designs for a 94 GHz Gyro-TWA employing the third or fourth cyclotron harmonic. Tables II and III list the design parameters. Within the context of the present model and assumptions, the main difficulty in achieving the projected efficiency appears to be the high sensitivity associated with the parameter X' ($\alpha B_0 / \gamma_0'$). As shown in Fig. 6, this parameter has to be tunable with an accuracy of $\sim 0.2\%$ for $s=3$ and $\sim 0.1\%$ for $s=4$. In the next section we discuss some difficulties not addressed in our model but which could be of overwhelming importance.

VI. DISCUSSION

The designs shown in Tables II and III all represent record microwave powers in the millimeter frequency range. Despite their attractiveness, it should be emphasized that these designs are of a preliminary nature because questions concerning the realization of our assumed cold beam single wave model remain unanswered. If such an idealized model is not realizable, one must determine how thermal effect and competitive mode effect, etc., alter the predicted efficiency. Here we briefly address these questions in a qualitative manner.

The validity of a cold beam model can be written in lab frame as¹⁶

$$\bar{k}_z \Delta\beta_z + s\bar{\Omega}_e \Delta\gamma/\gamma_0 \ll \left[\frac{v x_n H_s \beta_{10}^2}{4 \gamma_0 J_0^2(x_n)} \right]. \quad (53)$$

where $\Delta\beta_z$ is the axial velocity spread and $\Delta\gamma$ is the energy spread. On the basis of recent simulation studies of the magnetron-type electron gun¹⁶, we have found that condition (53) can be marginally satisfied for the first cyclotron harmonic. Since condition (53) becomes more restrictive for higher harmonics, it appears that further improvement of the electron gun design is required to generate a suitable electron beam. Also, thermal effects should be incorporated in future models because of their importance in higher harmonic operations.

We have examined the problem of competitive modes with a linear analysis¹⁷. All intersections of the waveguide mode characteristic curves with beam cyclotron harmonic curves were found to be unstable to some degree. The ones travelling backward could be classified as absolute instabilities and might present the greatest

danger. It should be stressed that it is not yet clear how seriously these modes will affect the device operation and further analysis is recommended. On the other hand, this problem serves to underline the advantage of beam position optimization discussed in Sec. II (item D). It has been shown¹⁷ that through such optimization the operating mode can at least have the highest growth rate as compared with all the competitive modes.

Finally, we point out that the beam space charge effects have not been examined in any detail in the present report. Presumably it will reduce the efficiency by introducing beam thermal and energy spread.

The authors would like to acknowledge many helpful discussions with T. Godlove, V. L. Granatstein, H. R. Jory, M. Read, J. L. Seftor, and P. Sprangle. In particular, we are very appreciative of the encouragement and critical comments of Dr. Granatstein. This work was supported by Rome Air Development Center, MIPR NO. FY761970026.

APPENDIX A
CONVERSION FORMULAE

For generality, numerical data are presented for beam frame normalized quantities. In this appendix, we tabulate the formulae needed to convert beam frame normalized quantities to lab frame physical quantities. Column 2 of Table IV converts the beam frame normalized quantities in column 1 to lab frame normalized quantities. The information needed for the conversion is the axial velocity v_{z0} (in lab frame) which defines the quantity γ_z in column 2,

$$\gamma_z \equiv [1 - v_{z0}^2/c^2]^{-1/2}.$$

Formulae presented in column 2 are based on the Lorentz transform. Derivations are obvious except for the following items.

$$(i) \quad n = n' \gamma_z (\gamma' - 1) / (\gamma_z \gamma' - 1) \quad (A.1)$$

To derive Eq. (A.1), we note that the wave energy per unit length is

$$W_f = \frac{KB_z^2 \omega_c^2}{8\pi\omega_c^2 c}$$

where K is a geometrical factor, B_z is the axial wave magnetic field amplitude, and ω_c is the waveguide cutoff frequency.

The beam kinetic energy per unit length is

$$W_b = N(\gamma - 1)mc^2$$

where N is defined in the text.

The lab frame efficiency (n) can therefore be written

$$n = \frac{W_f}{W_b} = \frac{KB_z^2 \omega_c^2}{8\pi\omega_c^2 c N(\gamma_0 - 1)} \quad (A.2)$$

In Eq. (A.2), K , B_z and ω_c are all frame independent quantities.

The beam frame efficiency (η') is also expressed by Eq. (A.2) with ω , N , and γ replaced by ω' , N' , and γ' respectively. Thus

$$\frac{\eta}{\eta'} = \frac{\omega^2 N' (\gamma' - 1)}{\omega'^2 N (\gamma - 1)} \quad (A.3)$$

Since $\omega = \gamma_z \omega'$, $\gamma = \gamma_z \gamma'$, and $N = \gamma_z N'$, substitution of these relations into Eq. (A.3) yields Eq. (A.1).

$$(ii) \quad \omega_r = \gamma_z \omega_r' \text{ and } \omega_i = \omega_i' / \gamma_z$$

In the beam frame, $k_z' = 0$. Hence all quantities vary as $\exp(-i\omega' t')$. To transform this expression into the lab frame, we use the relation $t' = \gamma_z (t - v_{z0} z/c^2)$ and obtain

$$\begin{aligned} \exp(-i\omega' t') &= \exp[-i(\omega_r' + i\omega') \gamma_z (t - v_{z0} z/c^2)] \\ &= \exp\left[-i\gamma_z \omega_r' t + i\frac{\gamma_z \omega_r' v_{z0}}{c^2} z + \gamma_z \omega_i' t - \frac{\gamma_z \omega_i' v_{z0}}{c^2} z\right]. \end{aligned}$$

Thus, the $\exp(-i\omega' t')$ dependence, viewed from the lab frame, has the following wave frequency (ω_r) and wave number (k_z),

$$\omega_r = \gamma_z \omega_r'$$

$$k_z = \gamma_z \omega_r' v_{z0} / c^2$$

and, if one follows a beam segment (i.e. let $z = v_{z0} t$), one observes a growth rate given by

$$\omega_i = \gamma_z \omega_i' (1 - v_{z0}^2/c^2) = \omega_i' / \gamma_z.$$

Column 3 converts the lab frame normalized quantities in column 2 to lab frame physical quantities. The conversion formulae are based on Eqs. (21)-(23) in the main text. The information needed at this step is the waveguide radius r_w , which can be determined from the desired wave frequency through

$$r_w = \bar{\omega}_r c / 2\pi f, \quad (A.4)$$

where $\bar{\omega}_r$ is the calculated wave frequency (normalized) and f is the desired wave frequency in Hz.

From the lab frame physical quantities in column 3, we can derive the beam current (I_b), beam power (P_b), and the maximum output wave power (P_w).

$$I_b = \nu mc^2 v_{zo} / e = 1.707 \times 10^4 \nu v_{zo} / c \text{ Amp}, \quad (A.5)$$

$$P_b = I_b (\gamma_0 - 1) mc^2 = 8.535 \times 10^6 \nu (\gamma_0 - 1) v_{zo} / c \text{ kW}, \quad (A.6)$$

$$P_w = \eta P_b. \quad (A.7)$$

REFERENCES

1. R.Q. Twiss, "Radiation Transfer and the Possibility of Negative Absorption in Radio Astronomy", *Australian J. Phys.* 11, 564-579, (1958).
2. J. Schneider, "Stimulated Emission of Radiation by Relativistic Electrons in Magnetic Field", *Phys. Rev. Lett.* 2, 504-505 (1959).
3. A.V. Gaponov, "Interaction Between Electron Fluxes and Electromagnetic Waves in Waveguides", *Izv. VUZ., Radiofizika* 2, 450-462 (1959) and "Addendum", *Izv. VUZ., Radiofizika* 2, 836 (1959).
4. V.A. Flyagin, A.V. Gaponov, M.I. Petelin and V.K. Yulpatov, "The Gyrotron", *IEEE Trans. MTT-25*, 514-521 (1977).
5. J.L. Hirshfield and V.L. Granatstein, "The Electron Cyclotron Maser - An Historical Survey", *IEEE Trans. MTT-25*, 522-527 (1977).
6. V.L. Granatstein, P. Sprangle, M. Herndon, R.K. Parker, and S.P. Schlesinger, "Microwave Amplification with an Intense Relativistic Electron Beam", *J. Appl. Phys.* 46, 3800-3805 (1975).
7. P. Sprangle and W.M. Manheimer, "Coherent Nonlinear Theory of a Cyclotron Instability", *Phys. Fluids* 18, 224-230 (1975).
8. P. Sprangle and A.T. Drobot, "The Linear and Self Consistent Nonlinear Theory of the Electron Cyclotron Maser Instability", *IEEE Trans. MTT-25*, 528-544 (1977).
9. A.V. Gaponov and V.K. Yulpatov, "Interaction of Helical Electron Beams with the Electromagnetic Field in a Waveguide", *Radio Eng. Electron. Phys.* 12, 582 (1967).

10. E. Ott and W.M. Manheimer, "Theory of Microwave Emission by Velocity-Space Instabilities of an Intense Relativistic Electron Beam", IEEE Trans. PS-3, 1-5 (1975).
11. K.R. Chu and J.L. Hirshfield, "Comparative Study of the Axial and Azimuthal Bunching Mechanisms in Electromagnetic Cyclotron Instabilities", Phys. of Fluids 21, 461-466 (1978).
12. B. Etlicher, A. Huetz, J.M. Buzzi, P. Haldenwang, and D. Lequeau, "Microwave Generation by Intense Relativistic Electron Beams Propagating in a Circular Waveguide", J. Applied Phys. (to be published).
13. K.R. Chu, A.T. Drobot, V.L. Granatstein, and J.L. Seftor, "Calculation of Optimum Operating Parameters for a Gyrotron Travelling Wave Amplifier", IEEE Trans. MTT (in press).
14. It is shown in Ref. 11 that if the beam thickness is small compared with the waveguide radius, the TE and TM modes, even degenerate, will remain decoupled.
15. K.R. Chu "Theory of Cyclotron Maser Interactions in a Cavity at Harmonic Frequencies", Naval Research Laboratory, Memo Report 3672 (to be published in Phys. of Fluids).
16. J.L. Seftor, A.T. Drobot, K.R. Chu, (to be published).
17. K.R. Chu and P. Sprangle, (to be published.)

Table I. Values of \bar{r}_0 for which $H_s(x_n r_0, x_n r_L)$ has an absolute maximum with respect to the argument $x_n \bar{r}_0$. The numbers marked by * have been used to obtain the data presented in Fig. 5 and also in simulation runs.

$n \backslash s$	1	2	3	4
1	0.48*	0.80		
2	0.26	0.43*	0.60	0.76
3	0.18	0.30	0.41*	0.52
4	0.14	0.23	0.32	0.40*
5	0.11	0.19	0.26	0.32
6	0.09	0.16	0.21	0.27
7	0.08	0.13	0.18	0.23
8	0.07	0.12	0.16	0.21

Table II. Efficiency optimized design parameters for a 94 GHz gyro-TWA operating at the third cyclotron harmonic. Data no refers to the points marked on Fig. 7.

data	no	1	2	3	4
v	($\times 10^3$)	2.05	2.08	5.12	5.19
W_b	(keV)	42.80	70.82	42.80	70.82
I_b	(Amp)	7.55	9.48	18.87	23.70
η	(%)	12.73	11.57	15.41	14.93
P_b	(kW)	323.1	671.5	807.8	1679.0
P_w	(kW)	41.2	77.7	124.5	250.7
B_0	(kG)	11.55	11.81	11.54	11.78
k_z	(cm^{-1})	4.25	5.27	4.25	5.27
r_w	(mm)	5.285	5.356	5.285	5.351
r_o	(mm)	2.182	2.212	2.182	2.209
r_L	(mm)	0.520	0.663	0.520	0.664
r_1	(mm)	1.663	1.549	1.662	1.545
r_2	(mm)	2.702	2.874	2.702	2.873
$v_{\perp 0}/c$		0.324	0.401	0.324	0.401
v_{z0}/c		0.216	0.268	0.216	0.268
g	(dB/cm)	1.167	1.583	1.844	1.855

Table III. Efficiency optimized design parameters for a 94 GHz gyro-TWA operating at the fourth cyclotron harmonic. Data no refers to the points marked on Fig. 8.

data	no	5	6	7	8
v	($\times 10^3$)	2.08	2.10	5.19	5.25
W_b	(keV)	70.82	98.49	70.82	98.49
I_b	(Amp)	9.48	10.93	23.70	27.32
n	(%)	6.67	6.96	8.87	9.25
P_b	(kW)	671.5	1076.0	1679.0	2691.0
P_w	(kW)	44.8	74.9	149.0	248.8
B_0	(kG)	8.878	9.085	8.872	9.070
k_z	(cm^{-1})	5.27	6.00	5.27	6.00
r_w	(mm)	7.017	7.093	7.011	7.093
r_o	(mm)	2.800	2.831	2.798	2.831
r_L	(mm)	0.881	1.028	0.882	1.030
r_1	(mm)	1.919	1.802	1.916	1.801
r_2	(mm)	3.681	3.859	3.680	3.861
v_{\perp}/c		0.401	0.457	0.401	0.457
v_z/c		0.268	0.305	0.268	0.305
g	(dB/cm)	0.738	0.779	0.930	1.130

Table IV. Formulae for transformation from beam frame into lab frame and for converting normalized quantities into physical quantities.

Beam Frame Normalized Quantities	Lab Frame Normalized Quantities	Lab Frame Physical Quantities
v'	$v = \gamma_z v'$	v (dimensionless)
γ'	$\gamma = \gamma_z \gamma'$	γ (dimensionless)
η'	$\eta = \eta' \gamma_z (\gamma' - 1) / (\gamma_z \gamma' - 1)$	η (dimensionless)
\bar{k}_z' ($= 0$)	$\bar{k}_z = \gamma_z \bar{v}_{z0} \bar{\omega}_r'$	$k_z = \bar{k}_z / r_w$
$\bar{\omega}_r'$	$\bar{\omega}_r = \gamma_z \bar{\omega}_r'$	$\omega_r = \bar{\omega}_r c / r_w$
$\bar{\omega}_i'$	$\bar{\omega}_i = \bar{\omega}_i' / \gamma_z$	$\omega_i = \bar{\omega}_i c / r_w$
$\bar{\Omega}_e'$	$\bar{\Omega}_e = \bar{\Omega}_e'$	$\Omega_e = \bar{\Omega}_e c / r_w$
\bar{r}_L'	$\bar{r}_L = \bar{r}_L'$	$r_L = \bar{r}_L r_w$
\bar{r}_o'	$\bar{r}_o = \bar{r}_o'$	$r_o = \bar{r}_o r_w$

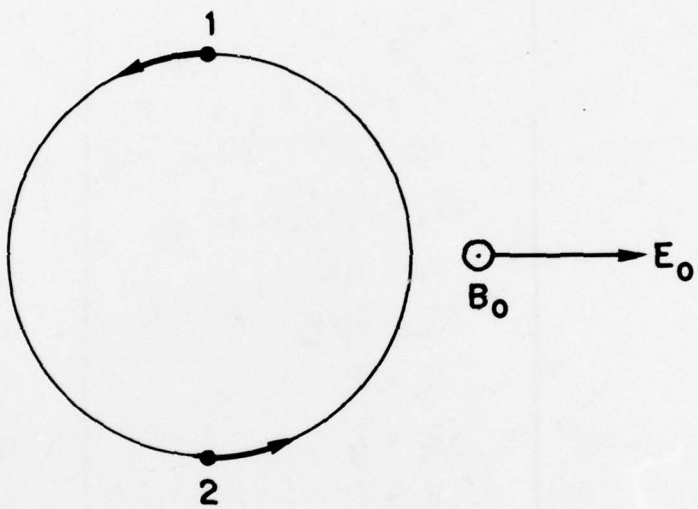


Fig. 1.

Instantaneous positions of two electrons circulating in the same cyclotron orbit, but separated by 180° in phase angle. E_0 is the wave electric field and B_0 (pointing toward the reader) is the applied magnetic field.

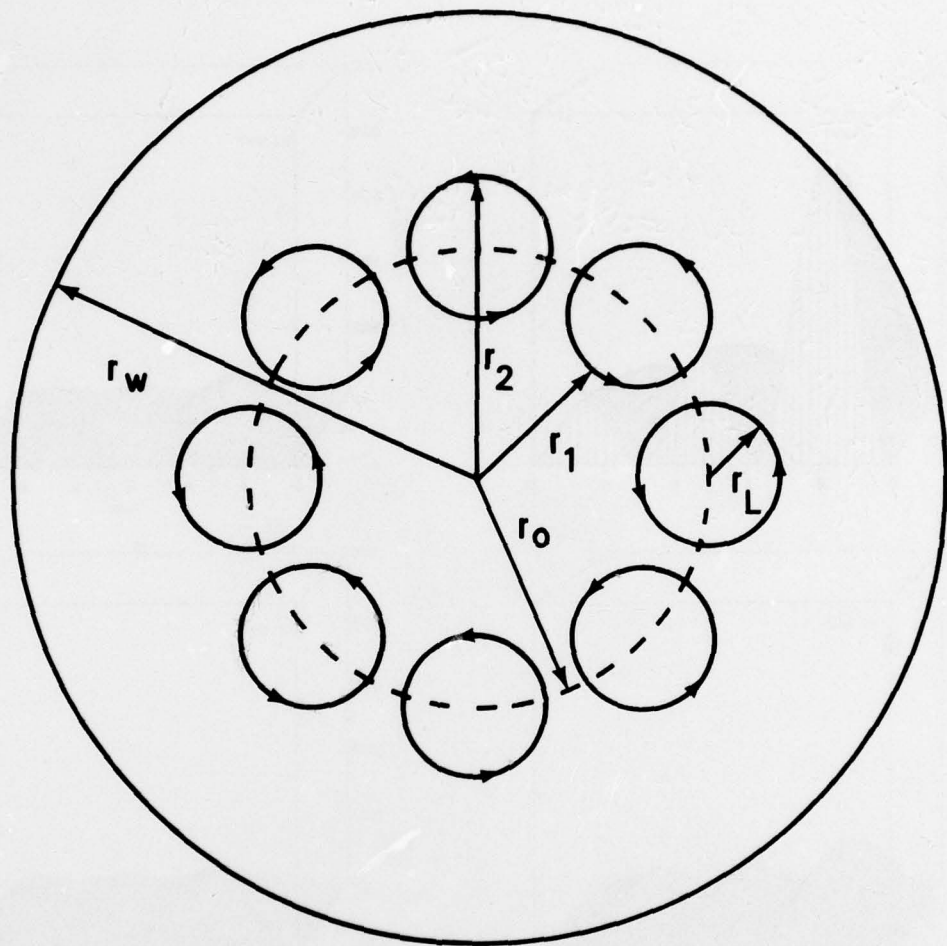


Fig. 2.

Cross-sectional view of the electron cyclotron maser model. The applied magnetic field (not shown) points toward the reader. The electrons are monoenergetic and all have the same Larmor radius r_L . Guiding centers of all electrons are uniformly distributed on the circle of constant radius r_0 .

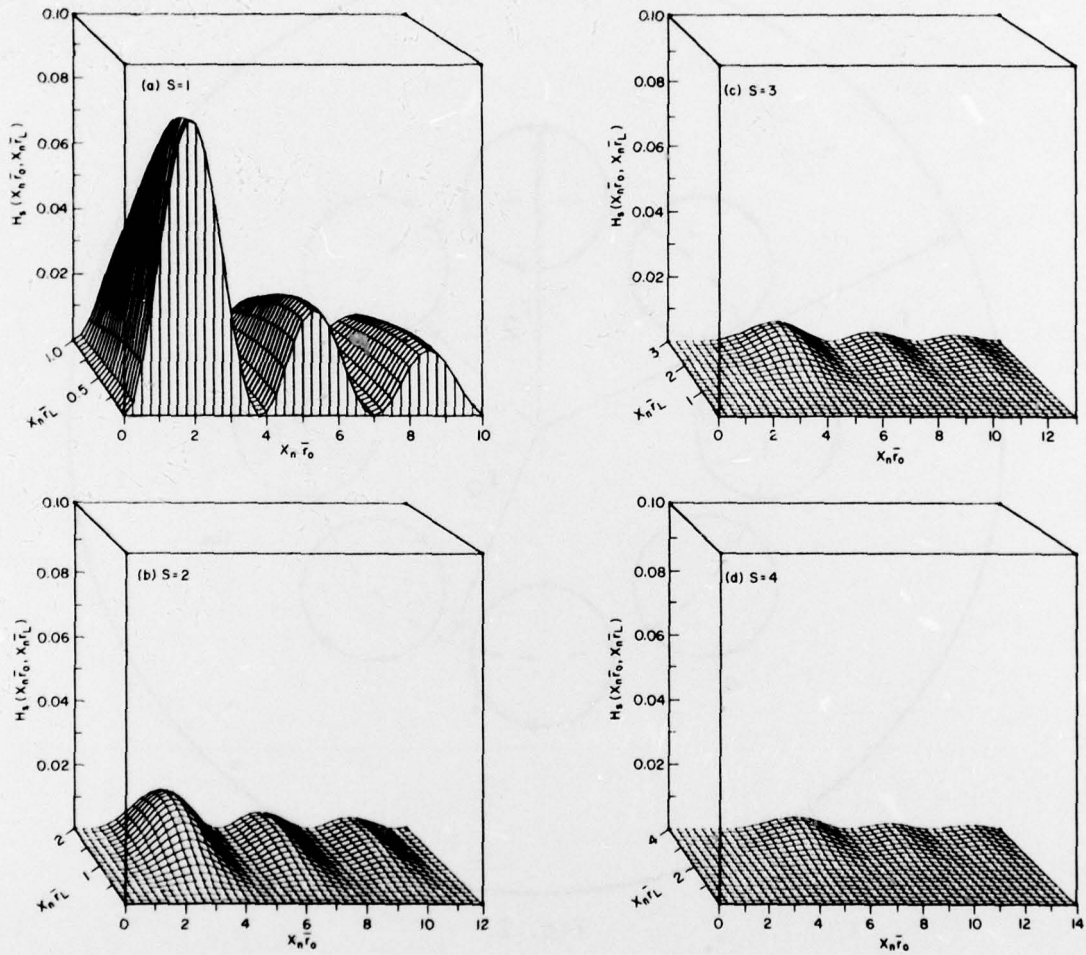


Fig. 3.

Plots of the beam-wave coupling coefficient $H_s(x_n \bar{r}_0, x_n \bar{r}_L)$ as a function of its arguments for the first four cyclotron harmonics.

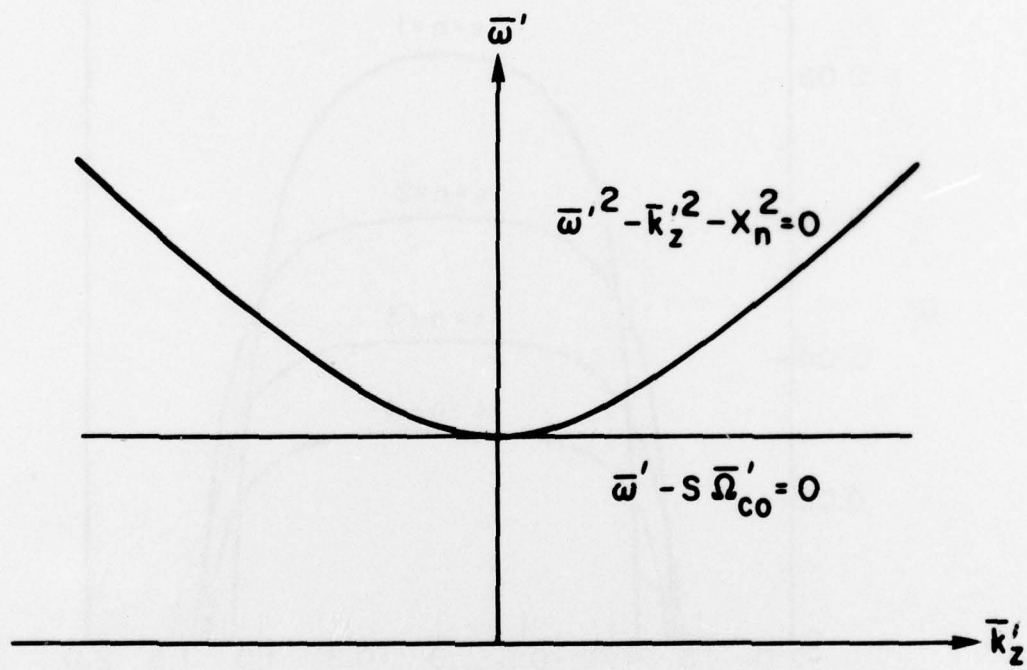


Fig. 4.

The vacuum wave guide characteristic curve and the beam characteristic curve in the $(\bar{\omega}', \bar{k}_z')$ plane (plotted in the beam frame).

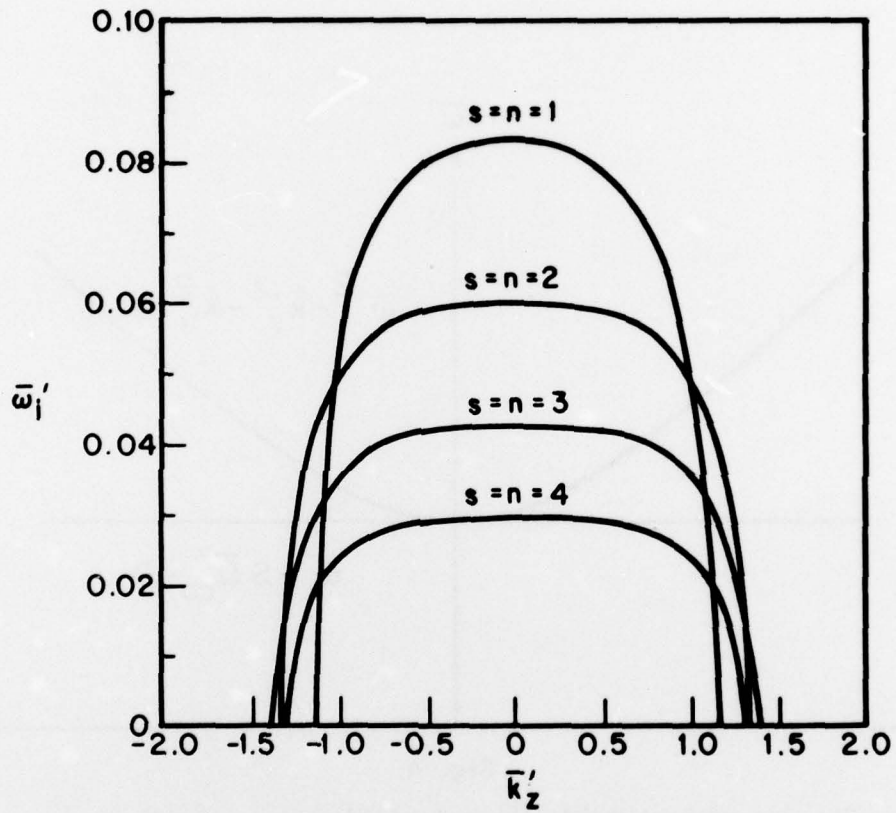


Fig. 5.

Growth rates ($\bar{\omega}_i'$) versus \bar{k}_z' for the first four cyclotron harmonics as computed from Eq. (25). Parameters used for this figure were $v' = 0.002$, $\gamma_0' = 1.1$ (50 keV), $X' = 1$, and $\bar{\gamma}_0 = 0.48, 0.43, 0.41, 0.40$ for $s = 1, 2, 3, 4$ respectively.

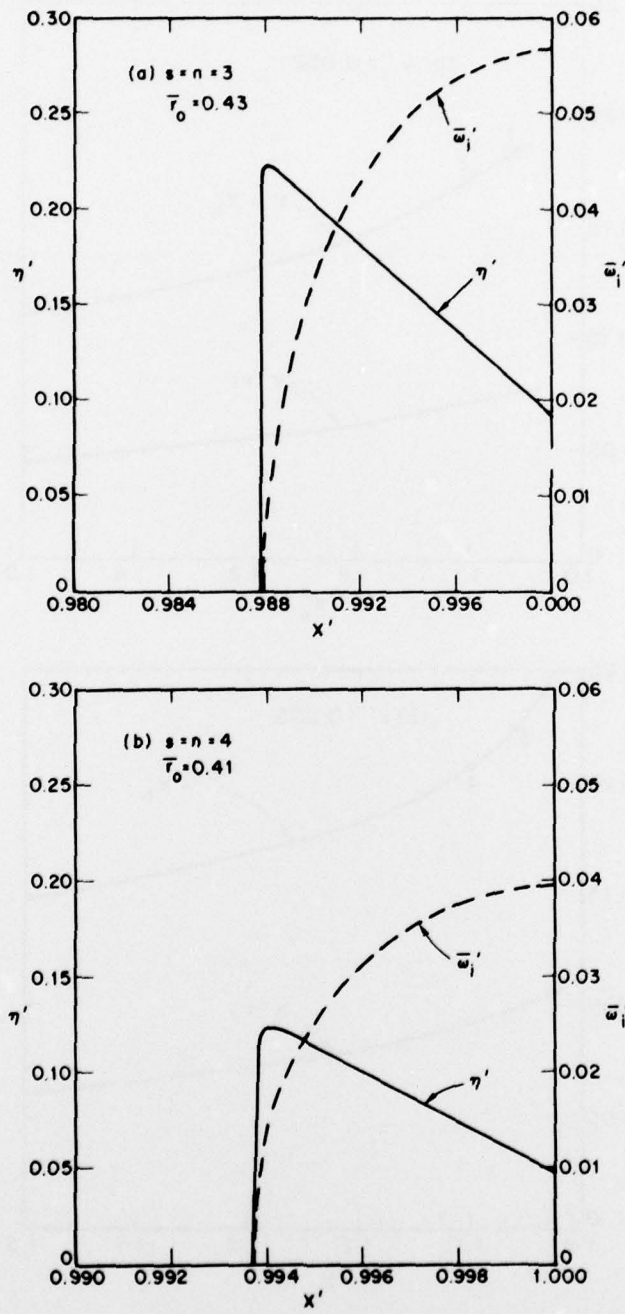


Fig. 6.

Efficiency (η') and growth rate ($\bar{\omega}'_i$) versus X' for $v' = 0.005$, $\gamma'_0 = 1.1$, and $\bar{k}'_z = 0$. These plots show the sensitivity of η' and $\bar{\omega}'_i$ to small variations in X' .

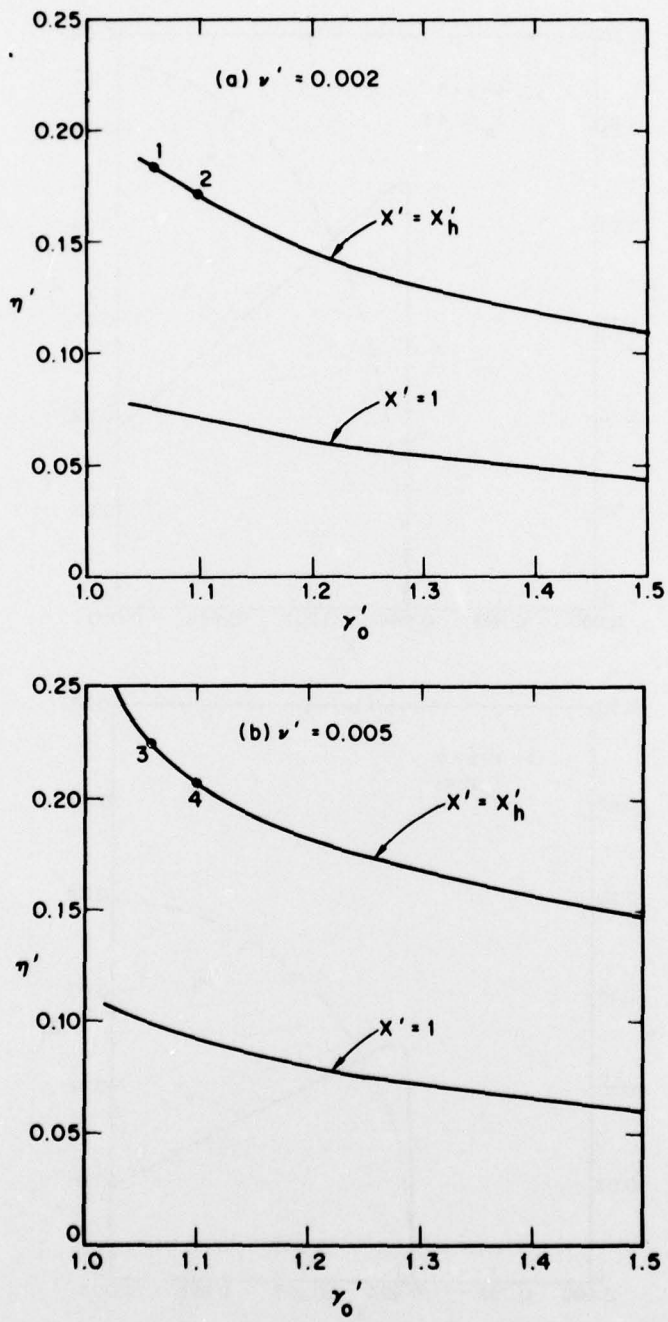


Fig. 7.

Efficiency (η) versus γ_0' for $s=n=3$, $\bar{r}_0=0.43$ and $\bar{k}_z'=0$. In each figure, the lower curve is for $X'=1$ (grazing intersection case) and the upper curve is for $X'=X_h'$ (half growth rate case).

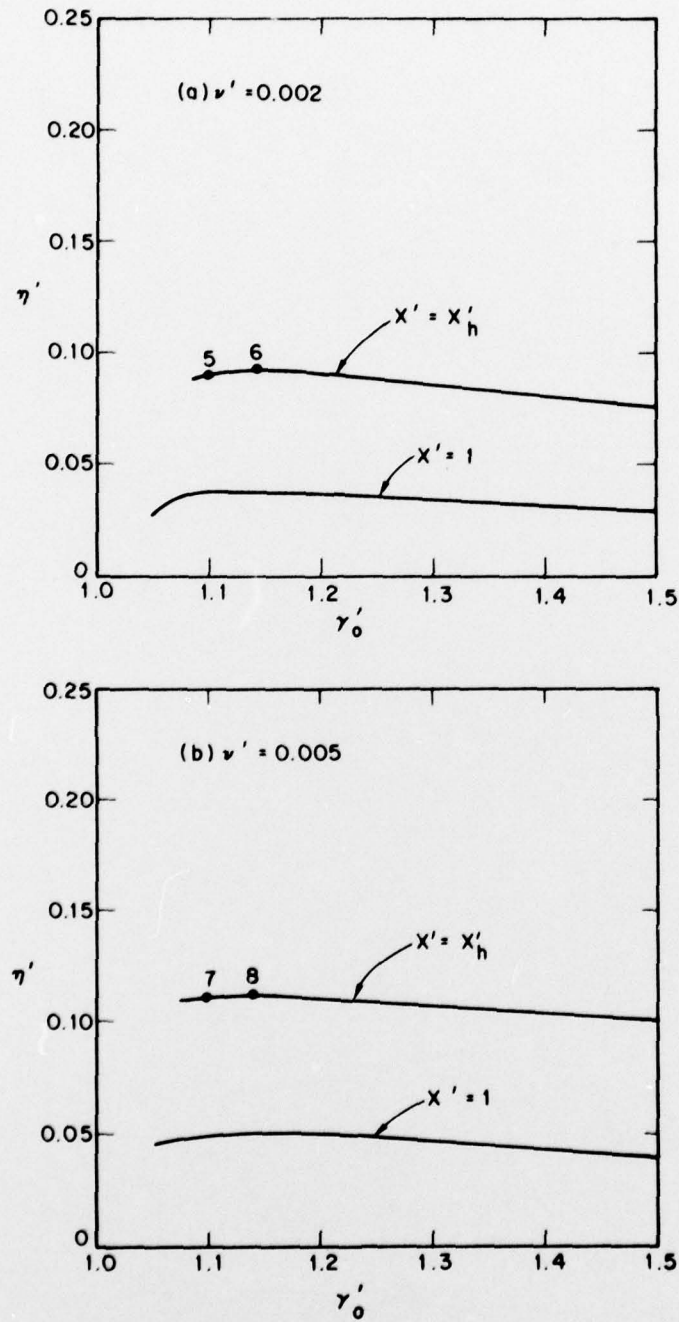


Fig. 8.

Efficiency (η') versus γ'_0 for $s=n=4$, $\bar{r}_0=0.41$, and $\bar{k}'_z=0$. In each figure, the lower curve is for $X'=1$ (grazing intersection case) and the upper curve is for $X'=X'_h$ (half growth rate case).